THE UNIVERSITY *of* EDINBURGH

Edinburgh Research Explorer

Semi-automated registration-based anatomical labelling, voxel based morphometry and cortical thickness mapping of the mouse brain

OPEN ACCESS

Research Article

Semi-automated registration-based anatomical labelling, voxel based morphometry and cortical thickness mapping of the mouse brain

Marco Pagani[1,2][¶][*], Mario Damiano[1][¶], Alberto Galbusera[1], Sotirios A Tsaftaris[3][&], Alessandro Gozzi[1][&][*]

[1] Center for Neuroscience and Cognitive Systems, Istituto Italiano di Tecnologia, Rovereto, Italy.

[2] Centro Interdipartimentale Mente/Cervello (CIMeC) - University of Trento, Rovereto, Italy.

[3] IMT Institute for Advanced Studies, Lucca, Italy.

[¶] *The two authors equally contributed to this work*
[&] *The two authors share senior authorship*

[*]**Corresponding Authors:**

e-mail: alessandro.gozzi@iit.it
e-mail: marco.pagani@iit.it

Highlights

- We describe registration-based methods for mouse brain morphoanatomical imaging.
- Detailed workflows for anatomical labelling, voxel based morphometry and cortical thickness are reported.
- The same preprocessing can be applied to map multiple complementary anatomical readouts.
- The present work may help to promote the use of rodent morphoanatomical imaging.

1   **Abstract**

2   *Background*

3   Morphoanatomical MRI methods have recently begun to be applied in the mouse. However,

4   substantial differences in the anatomical organisation of human and rodent brain prevent a

5   straightforward extension of clinical neuroimaging tools to mouse brain imaging. As a result, the

6   vast majority of the published approaches rely on tailored routines that address single

7   morphoanatomical readouts and typically lack a sufficiently-detailed description of the complex

8   workflow required to process images and quantify structural alterations.

9   *New method*

10   Here we provide a detailed description of semi-automated registration-based procedures for

11   voxel based morphometry, cortical thickness estimation and automated anatomical labelling of

12   the mouse brain. The approach relies on the sequential use of advanced image processing tools

13   offered by ANTs, a flexible open source toolkit freely available to the scientific community.

14   *Results*

15   To illustrate our procedures, we described their application to quantify morphological alterations

16   in socially-impaired BTBR mice with respect to normosocial C57BL/6J controls, a comparison

17   recently described by us and other research groups. We show that the approach can reliably

18   detect both focal and large-scale gray matter alterations using complementary readouts.

19   *Comparison with existing methods*

20   No detailed operational workflows for mouse imaging are available for direct comparison with

21   our methods. However, empirical assessment of the mapped inter-strain differences is in good

22   agreement with the findings of other groups using analogous approaches.

23   *Conclusion*

24   The detailed operational workflows described here are expected to help the implementation of

25   rodent morphoanatomical methods by non-expert users, and ultimately promote the use of these

26   tools across the preclinical neuroimaging community.

27

1. Introduction

A deep understanding of the genetic, physiological and anatomical underpinnings of brain disease is essential for the development of improved therapies. A milestone towards this goal is the generation of genetically modified mouse lines that recapitulate targeted genetic mutations in experimentally controlled studies. Genetically modified mouse lines permit to relate genetic mutations to clinically relevant endophenotypes without the complexity of genetic heterogeneity and the uncontrolled impact of gene-gene and gene-environment interactions in adult human populations (Nestler and Hyman, 2010).

Magnetic resonance imaging (MRI) methods offer a privileged point of view to study genetically altered mouse models of neuropsychiatric disorders in many respects. First, the use of comparable imaging readouts in men and mice permits a cross-species comparison of brain endophenotypes of translational relevance, thus enhancing the transfer of information from and to the clinic. At the same time, MRI readouts can also be employed to assess the extent to which mouse models of central nervous system pathology replicate neuroimaging findings observed in clinical populations, informing preclinical researchers on the translational validity of these models. Moreover, high resolution morphometric MRI, achievable at ultra-high field strength or in *ex vivo* formalin-fixed samples (Lerch et al., 2012; Tucci et al., 2014) can be employed to obtain a fine-grain assessment of structural brain alterations that could serve as a convenient surrogate for labour intensive manual morphometric measurements in *ex vivo* brain slice preparations, with the additional advantage of being non-invasive and multi-dimensional.

Structural MRI based imaging methods - such as voxel based morphometry (VBM) of gray matter (GM), cortical thickness mapping and anatomical labelling - have been widely employed to study brain morphology in human populations (Mueller et al., 2012). The application of analogous readouts to map genetically determined brain alterations in transgenic mouse lines has been recently proposed, an effort collectively referred to as MRI phenotyping (Borg and Chereul, 2008; Johnson et al., 2007; Lerch et al., 2011a). Recent improvements in MRI sequences and hardware, together with the development of fixation protocols for *ex vivo* imaging of stained brain specimens (Lerch et al., 2012), have made it possible the acquisition of artefact-free and high resolution – with a voxel size less than 80 μm – mouse brain volumes even at relatively low magnetic field strengths. This efforts have resulted in the publication of several examples or the application of morphoanatomical imaging to transgenic mouse models (Lerch et

62   al., 2008; Sawiak et al., 2009; Xie et al., 2010; Yushkevich et al., 2006).

63   The development of standardised preprocessing and analytical pipelines for human

64   imaging data, and their implementation in popular software toolkits such as such as FMRIB

65   Software Library (FSL) (Jenkinson et al., 2012), Statistical Parametric Mapping (SPM) (Friston

66   et al., 1994) and Advanced Normalization Tools (ANTs) (Avants et al., 2009), have been

67   instrumental to the widespread use of MRI in human brain research. However, substantial

68   differences in the dimensions and anatomical organisation of the human and rodent brain prevent

69   a straightforward extension of these tools to morphoanatomical mouse brain mapping. As a

70   result, several research groups have developed tailored procedures for the preprocessing and

71   analyses of morphoanatomical brain MRI readouts in mouse models (Badea et al., 2012; Borg

72   and Chereul, 2008; Delatour et al., 2006; Johnson et al., 2007; Lee et al., 2010; Lerch et al.,

73   2011a; Nieman et al., 2005; Sawiak et al., 2009; Sawiak et al., 2013). However, the vast majority

74   of the published approaches typically address single morphoanatomical readouts (e.g., VBM *or*

75   anatomical labelling *or* cortical thickness), and lack a detailed description of the complex

76   workflow and computational parameters required to process, analyse and quantify structural MRI

77   alterations, thus complicating the implementation of these procedures by non-expert users.

78   To begin to address these issues, here we provide a detailed methodological description

79   of a semi-automated operational workflow for VBM, cortical thickness estimation and automated

80   anatomical mapping of the mouse brain. To simplify and streamline operations, we based image

81   processing mainly on ANTs (Avants et al., 2009), a flexible and powerful open source toolkit

82   freely available to the scientific community. Importantly, our approach has been recently applied

83   by our research group to map fine-grain brain anatomy alterations in different mutant mouse

84   lines (Dodero et al., 2013; Lassi et al., 2015; Minervini et al., 2014; Sannino et al., 2014; Tucci et

85   al., 2014) and to describe large-scale networks of anatomical covariance between gray matter

86   regions in wild-type mice (Pagani et al., 2016), with excellent agreement between MRI and

87   manual morphometric measurements (Sannino et al., 2014), exhibiting corresponding

88   morphoanatomical features in mice and reference clinical populations (Cutuli et al., 2016; Tucci

89   et al., 2014). Below, we provide a detailed description of our procedural workflow and show its

90   capabilities by describing its application to quantify morphological alterations in socially-

91   impaired BTBR T+Itpr3tf/J mice with respect to normo social C57BL/6J controls (Dodero et al.,

92   2013; Squillace et al., 2014), a comparison that has been recently described by our research

93   group (Dodero et al., 2015) and others (Ellegood et al., 2013), thus permitting an empirical cross-

94   laboratory assessment of the validity of our findings.

95

96   **2. Materials and Methods**

97

98   **2.1. Ethical statement**

99   All *in vivo* studies were conducted in accordance with the Italian law - D.L. n° 116, 1992,

100   Ministero della Sanità, Roma - and following the recommendations in the Guide for the Care and

101   Use of Laboratory Animals of the National Institutes of Health. The animal research protocol

102   was approved by the Animal Care Committee of the Istituto Italiano di Tecnologia (Permit Date

103   07-2012). All surgical procedures were performed under deep anaesthesia.

104

105   **2.2. Sample Preparation and MR acquisition**

106   High-resolution morphoanatomical T2-weighted MR imaging of mouse brains was

107   performed in paraformaldehyde (4% PFA; 100 ml, Sigma, Milan) fixed specimens, a procedure

108   employed to obtain high-resolution images with negligible confounding contributions from

109   physiological or motion artefacts (Cahill et al., 2012). Sample preparation and MRI acquisition

110   of BTBR T+Itpr3tf/J (BTBR) and C57BL/6J (B6) mice has been recently described in previous

111   work (Dodero et al., 2013; Sforazzini et al., 2014a; Sforazzini et al., 2014b) and is briefly

112   summarised here. Male BTBR (N=9, 15-26 weeks old) and age-matched control B6 (N=9) mice

113   were deeply anaesthetized with an intraperitoneal Avertin injection (375 mg/Kg, Sigma, Milan)

114   and their brains were perfused *in situ* via cardiac perfusion. The perfusion was performed with

115   phosphate buffered saline followed by paraformaldehyde (4% PFA; 100 ml). Both perfusion

116   solutions were added with a Gadolinium chelate (Prohance, Bracco, Milan) at a concentration of

117   10 and 5 mM, respectively, to shorten longitudinal relaxation times (Lerch et al., 2012).

118   A multi-channel 7.0 Tesla MRI scanner (Bruker Biospin, Milan) was used to acquire

119   anatomical images of the brain, using a 72 mm birdcage transmit coil, a custom-built saddle-

120   shaped solenoid coil for signal reception, and the following imaging parameters: 3D RARE spin-

121   echo sequence, TR=550 ms, TE=33 ms, RARE factor=8, echo spacing 11ms, matrix size of 192x

122   170x170 and voxel size of 0.09 mm (isotropic), with a total acquisition time of 4 hrs and 25

123   mins.

2.3. Image preprocessing and analysis

124

125

126   A detailed description of the image processing workflow employed to create a study

127   based template, to estimate cortical thickness, and to perform automated anatomical labelling and

128   VBM is reported below for structural images acquired at 7 Tesla. We refer to our approach as

129   "registration-based" as several preprocessing and estimation steps (e.g., cortical thickness) are

130   executed via a combination of affine and symmetric diffeomorphic transformations as

131   implemented in *antsRegistration* command (Avants et al., 2014). The tool entails the application

132   of affine registration with twelve degrees of freedom to coarsely normalise the overall shape of a

133   source image to a reference image. Afterwards, a non-linear transformation is applied to create a

134   differentiable and invertible diffeomorphic map which locally aligns source and reference image

135   by adjusting for local inter-individual morphological differences.

136   Flowcharts are provided as a visual reference to guide the description of each

137   computational step, where light grey shading denotes image inputs, dark grey shading denotes

138   the final output and computational processes are outlined in the form of rectangular boxes. All

139   the computational steps have been carried out using tools and algorithms implemented within the

140   ANTs toolkit (version 1.9 http://sourceforge.net/projects/advants/) and employed to process 3D

141   RARE morphoanatomical images acquired at 7 Tesla with the image sequence parameters

142   described above. The parameter employed for the preprocessing steps were optimized in pilot

143   assessments using both empirical (e.g. segmentation) and quantitative approaches (e.g.

144   registration).

145

146   *2.3.1. Image preprocessing*

147   Basic image preprocessing includes bias field correction and skull stripping (Figure 1).

148   As a first step, all the images are corrected for intensity non-uniformity using

149   *N3BiasFieldCorrection*, an automated algorithm implemented within the ANTs toolkit using 50

150   fitting levels. This step reduces bias field signal related to the reception profile of MRI receive

151   coils, a low frequency amplitude modulation of the signal that produces regional variation in

152   voxel intensity as a function of coil proximity. The correction of this bias is an important pre-

153   requisite for subsequent intensity based MR image processing, such as tissue segmentation.

154   Skull stripping is required to remove extra brain tissue, thus crucially improving the

155 accuracy of subject-to-template registration. In order to automate skull-stripping and avoid

156 tedious and error-prone manual segmentation, an automatic registration-based approach to skull

157 stripping was devised. This is carried out by registering the bias adjusted MRI volumes to a skull

158 stripped reference image using an affine and diffeomorphic registration algorithm. The skull

159 stripped reference image should ideally be chosen from the study population or from comparable

160 experiments of the same laboratory. A companion brain binary mask of the reference image can

161 be segmented manually. While potentially labour intensive in high resolution brain images, this

162 process can be performed only once, and it is instrumental to automating skull stripping for all

163 the subsequent subjects and analyses. After the registration, the diffeomorphic map is applied to

164 non-linearly transform the brain mask of the reference image into the subjects' space using

165 *WarpImageMultiTransform.* The subject's brain mask is then applied to each original subject

166 image to obtain skull stripping. An additional bias correction is subsequently performed on the

167 skull stripped subject image to achieve a more accurate estimation of the bias field, devoid of the

168 contribution of non-brain related protrusions.

169 An illustrative example of the advantage of performing two independent bias corrections,

170 (before and after skull stripping, respectively) is reported in Figure 2. Even though the first step

171 does not flawlessly compensate for signal inhomogeneity in all brain regions (i.e. the ventral

172 areas of the brain and in the ventricles), its use provides a first normalization of signal intensity

173 that results in an improved the accuracy of registration based estimation of brain mask, and the

174 removal of brain extra tissue. After this skull stripping step, the bias field of the original subject

175 image is re-estimated, leading to a more accurate bias correction. The results of this first-pass

176 skull stripping are typically visually inspected for imperfections, usually present in a minority of

177 subjects, which can be easily manually corrected, for example using the brushtool of ITKsnap

178 (Yushkevich et al., 2006). For each subject, the result of preprocessing is a skull stripped and

179 bias corrected brain image, exhibiting uniform contrast within the same tissue class, and its

180 binary mask.

181

182 *2.3.2. Study based template*

183 A critical element in our approach is the construction of a study based template to

184 establish a common reference space for all the subsequent analyses. In cross-sectional mouse

185 studies, the most adopted experimental designs for mouse phenotyping with transgenic lines, this

186   involves the creation of an average template from a reference population, typically the control

187   subjects (B6 in this study). This leads to the generation of a template recapitulating

188   neuroanatomical features of "healthy" or reference population, avoiding the combination of

189   conflicting morphoanatomical traits which could affect subsequent computational steps (e.g.

190   segmentation). For example, the use of both normo-callosal B6 and acallosal BTBR mice for

191   template creation would result in a chimeric image exhibiting a blurred and hypo-intense corpus

192   callosum, a feature that could negatively affect the quality of subsequent segmentation priors.

193   The creation of different templates for different studies can help minimizing confounding effects

194   related, for instance, to perfusion, age, sex and brain sizes.

195   Study-based template creation was implemented via the use of the *buildtemplateparallel*

196   script available within the ANTs toolkit (Avants et al., 2010b). This script entails an automated

197   and iterative intensity-based registration approach to automatically create a study based template

198   using a predefined list of subjects (Kovacevic et al., 2005). A representative subject is selected as

199   initial reference and each subject is linearly registered to the reference subject using an affine

200   transformation. After intensity averaging all registered images to obtain a first linear group

201   average, an iterative five-generation multi-scale non-linear alignment process is performed using

202   a *Greedy Syn* diffeomorphic registration algorithm (Avants et al., 2008) with a maximum of 120

203   iterations for each step. This process entails an initial diffeomorphic registration of each subject

204   to the reference linear group average to obtain individuals' warps using cross correlation as

205   similarity metric. These warps are then averaged and applied to the template to update its shape

206   and conform it to the population shape. The process is iteratively repeated four more times, by

207   using as reference the warped template from the previous iteration. The final outcome is an

208   average template volume exhibiting clear structural boundaries, incorporating fine grain

209   neuroanatomical descriptions of the reference population, and reduced intensity variation.

210

211   *2.3.3. Anatomical labelling*

212   The assessment of subtle anatomical differences in gross morphology via manual delineation

213   of brain structures is a laborious and time consuming task that may introduce intra- and inter-

214   observer bias (Badea et al., 2012). The procedures described here allows for volumetric

215   estimation via anatomical labelling, a procedure whereby brain regions can be labelled and

216   classified depending on their anatomical location. The process employed in our workflow relies

217 on the availability of preprocessed images, a study-based template and two neuroanatomical

218 labelled reference MRI atlases for cortical (Ullmann et al., 2013) and subcortical (Dorr et al.,

219 2008) areas, respectively. The output of automated anatomical labelling is a fine-grained

220 projection of a given anatomical label in the subject's coordinate space. The anatomical labels

221 thus registered can be used both to measure the volume of anatomical regions of interest for

222 cross-strain statistical comparison, or as intermediate input for further analyses, such as cortical

223 thickness estimation (Figure 3).

224   The volume of specific anatomical regions in individual subjects is computed using a

225 template based anatomical labelling strategy (Avants et al., 2010b). As previously reported in

226 the literature, the propagation of labels from the anatomical labelled atlas to the subject space is

227 more accurate when performed via the study based template to minimize variation due to

228 registration errors (Jia et al., 2011). To this purpose, a composition of affine and diffeomorphic

229 (SyN) registration between the reference neuroanatomical atlas and the study based template is

230 performed to project the anatomical labels in the coordinate system of the study based template

231 (Avants et al., 2009) For the anatomical images and RARE sequence used in this study we

232 adopted cross correlation as similarity metric, with a window radius of 5 and a gradient step

233 length of 0.25. The optimisation was performed over four resolutions for both transformations

234 with a maximum of 100 iterations for the coarse levels and 10 at the full resolution. A simple

235 propagation of the neuroanatomical labels mapped in the study-based template space to the

236 subjects' space can then be achieved via the registration of each subject to the study based

237 template and the subsequent propagation of the labels to each subject. The efficiency of the

238 registration procedures can evaluated using the Dice coefficient (*DiceAndMinDistSum* command

239 from *ImageMath)*, which quantifies the overlap between a manually defined label and the same

240 label resulting from our automated labelling, in the subject space (Dice, 1945). Label volumes

241 can then be easily computed using tools included in several MRI software packages (e.g.

242 *LabelStats* command from *ImageMath*, or FSL's *fslstats*).

243

244 *2.3.4. VBM*

245   VBM is a whole-brain technique for characterizing regional brain volume and differences

246 in tissue concentration, in particular GM, across subjects. In our procedure, it consists of five

247 main steps (Figure 4).

248   First, a study based template is created using brain anatomical images from reference

249   population described above. Second, the original images of the two groups of subjects are

250   registered to the study based template via the same affine and diffeomorphic mapping used for

251   anatomical labelling. Third, spatially normalized images are segmented using a Markov Random

252   Field model, implemented by the *Atropos* command of the ANTs toolkit (Avants et al., 2011).

253   To classify tissues we applied a smoothing factor of 0.0125, a radius of 1 and the maximum

254   number of iterations was set at 10. The separation of GM (i.e. the readout of interest) from white

255   matter (WM) and cerebrospinal fluid (CSF) is improved by initializing the process with the study

256   based template, previously segmented using standard k-means clustering included in the *Atropos*

257   command. (Figure 5, B-C). This step is especially critical and it is therefore here described in

258   greater detail. In pilot work, we explored the number of tissue classes leading to optimal

259   separation of GM from non-GM components (WM plus CSF). A canonical three-class

260   segmentation of *ex vivo* mouse brain using *Atropos* results in inefficient GM/WM segmentation,

261   leading to an overestimation of WM fraction at the expense of GM (Figure S1). The use of six

262   independent classes results in three GM clusters that can be merged to provide a final accurate

263   GM map (Fig. 5). A similar approach has been employed by other investigators (e.g. (Li et al.,

264   2009)). Our segmentation procedure results in a two-voxel layer on the outmost edge of the

265   cortex which is labelled as "non gray matter" and, as such, is not included in subsequent

266   analysis. These voxels are characterised by low or very-low signal intensity and reflect a

267   combination of partial volume effects between gray matter and non MRI visible skull signal, and

268   possibly also small inaccuracies due to registrations. In our workflow, these "low confidence"

269   gray matter voxels are discarded to improve the robustness of subsequent voxelwise statistical

270   mapping.

271   In our procedure, the quality of segmentation is assessed empirically by comparing

272   individual and merged tissue classes with the anatomical distribution of known high-density WM

273   structures such as the corpus callosum, anterior and posterior commissures, as seen in the study

274   based template (Figure 5). These structures are easily identifiable and their extension can be

275   compared with their segmented counterparts. Future developments of our initial workflow could

276   employ quantitative approaches to estimate goodness of cluster separation (Chou et al., 2004;

277   Wu and Yang, 2005), although operator dependent assessments of tissue class separations are

278   ultimately warranted to ensure biologically meaningful results.

279   It should be noted that the segmentation procedure employed in our work does not always
280   lead to a clear separation of WM and CSF, at least on brain volumes acquired *ex vivo*. Besides
281   differences in the anatomical organization of the mouse brain and image contrast in the PFA
282   perfused brain (Cahill et al., 2012), a contributing reason for this is the occurrence of CSF loss
283   from the brain in a large proportion (ca. 70%) of the subjects as a consequence of the *ex vivo*
284   fixation procedure, leading to the presence of signal voids in ventricular space. These low signal-
285   intensity intra-ventricular foci are typically classified as WM, leading to mixed or incomplete
286   separation between these two brain components. Such incomplete separation however does not
287   limit the validity of our approach, because both CSF and WM (even if separate) would invariably
288   end up being discarded from subsequent GM-based analyses (i.e. VBM and cortical thickness).
289   After tissue segmentation, the Jacobian determinants of the deformation are calculated with
290   *ANTSJacobian* command of the ANTs toolkit and used to modulate the GM probability maps
291   calculated during the segmentation step. This step permits the analysis of GM probability maps
292   in terms of local anatomical variation instead of tissue density (Ashburner and Friston, 2000).
293   Jacobian determinants can be also normalized by the total intracranial volume to further
294   eliminate overall brain volume variations and calculate relative GM volumes. Fifth, the resulting
295   modulated GM probability maps are smoothed using a Gaussian kernel with a sigma of three
296   voxel width (FWHM=0.64mm) and employed for voxel-wise statistical comparison.

297

298   *2.3.5. Cortical Thickness*

299   The proposed registration-based cortical thickness *DiReCT* estimation approach (Figure
300   3) is a voxelwise computational approach based on the method presented by Das and colleagues
301   (Das et al., 2009) and relies on the *KellyKapowsky* command within ANTs toolkit. The method
302   provides cortical thickness measurements at the voxel level using cortical and non-cortical
303   labelled volumes as inputs. From an anatomical standpoint, the cortical labelled volume
304   employed (cortical ribbon) is limited between an external outline corresponding to the outer
305   layer of the cortex and an internal outline identified by the inner layer of the cerebral cortex
306   adjacent to callosal WM fibres. The method identifies a continuous one-to-one correspondence
307   between inner and outer cortical surfaces and the cortical thickness is estimated via a distance
308   measure on the basis of this diffeomorphic correspondence. The inner surface is used as a
309   reference to initialize a thin layer of about 1 voxel width. This layer, which replicates the shape

10

310 of the outer layer of the cortex, is then allowed to expand under the diffeomorphic deformation.

311 The deformation is introduced through the cortical label until the layer reaches the outer cortical

312 surface and the obtained deformation map can eventually be used to compute the cortical

313 thickness. The final result of this process is a cortical voxelwise map with a nominal "thickness"

314 value in each voxel, reflecting the deformation field that voxel has been subjected to (Das et al.,

315 2009). Figure S2 shows an illustrative example of the obtained voxelwise cortical thickness map

316 where the presence of parallel columns of voxels exhibiting constant thickness is apparent. The

317 obtained maps are then typically cross-compared using standard voxelwise statistics. The

318 original method (Das et al., 2009) was optimized to identify deep sulci of the human brain by

319 forcing the algorithm to recover lost sulci, but can also be applied to map lissencephalic cortices

320 like those of the rodent brain. The estimation process is carried out separately for right and left

321 hemisphere to preserve the Neumann boundary (Lee et al., 2011).

322 The cortical thickness estimation includes four main steps. First, a right and the left

323 cortical label need to be created, as well as the non-cortical label. In the present study this was

324 achieved by combining all cortical labels mapped (enthorinal cortex, frontal, occipital and

325 parieto-temporal lobe) of the Dorr MRI atlas of the mouse brain (Dorr et al., 2008) into one

326 single hemispheric label. A non-cortical label was generated by merging all the remaining non-

327 cortical regions. Second, cortical thickness is estimated using *KellyKapowsky*, with a prior

328 anatomical constraint of cortical thickness of two millimetres and a gradient step size for

329 optimisation of 0.02. Number of iterations, threshold and window size for convergence were left

330 unchanged (e.g. default parameters). Third, maps of cortical thickness are combined into a joint

331 volume and transformed to template space using available registration maps obtained previously.

332 Fourth, the transformed cortical maps are smoothed using a Gaussian kernel with a sigma of two

333 voxel width (FWHM=0.42). This process yields images that can be used for univariate or

334 multivariate analysis at the voxel level.

335 Despite the use of non-callosal mice our automated anatomical labelling correctly

336 labelled the cortical mantle of BTBR in virtually all cortical areas, with possible minor

337 underestimations of cortical thickness in medial anterior cingulate regions. As a result,

338 intergroup alterations in those regions may be interpreted cautiously when acallosal mice are

339 used as reference strain. However most mouse lines commonly used in neuroscience and

340 preclinical research exhibit normal callosal integrity and are therefore to be considered immune

341   to this potential artefact.

342   To further evaluate the accuracy of the cortical thickness estimation process, manual

343   measurement was also performed by an experienced operator blinded to the results of the cortical

344   thickness estimation (Figure 6). In a randomly chosen subject, three coronal slices were extracted

345   and cortical thickness was measured for secondary motor cortex (M2), secondary somatosensory

346   cortex (S2) and auditory cortex (Au) using the ruler tool available in the ITK Workbench.

347

348   **2.4. Statistical analysis**

349   All statistical analysis of the smoothed and modulated GM probability maps and cortical

350   thickness maps were conducted using FSL. Firstly, maps were concatenated in a 4D dataset,

351   using *fslmerge*. Subsequently, standard non-parametric Monte Carlo test with 5000 random

352   permutations was performed using *randomise*. Threshold-free cluster enhancement was

353   employed to include voxels' neighbourhood information without defining a-priori cluster

354   threshold. P-values were corrected for multiple comparisons using a cluster-based threshold of

355   0.01 (Jenkinson et al., 2012; Worsley et al., 1992). Two-tailed voxelwise statistics were used for

356   inter-group VBM and cortical thickness mapping. Brain volumes, resulting from the

357   segmentation process, were tested for statistical differences between the two strains using a two-

358   tailed Student's t-test, followed by Hochberg's correction for multiple comparisons.

359

360   **3. Results**

361   As an illustrative example of the approach, we tested our set of methods to map and

362   quantify morphological variations in inbred socially impaired BTBR mice with respect to

363   normosocial B6 (Squillace et al., 2014). A biological interpretation of the differences mapped

364   has been recently reported by us (Dodero et al., 2013) and others (Ellegood et al., 2013), and will

365   not be re-discussed here.

366

367   *3.1. Study based template and volumetric analysis*

368   A study based template created following the procedure herein explained is depicted in

369   Figure 5. The template was created using the scans of nine normosocial B6 mice, which have

370   been used as reference population for this illustrative study. The template reveals clear structural

371   boundaries and high WM-GM contrast, depicting fine-grain anatomical features that can be used

12

372   to describe the population more effectively and reliably than a single representative subject

373   (Tucci et al., 2014).

374   In pilot studies, we assessed the accuracy of registrations as a function of varying

375   registration parameters (i.e. window radius and gradient step for symmetric normalization) as

376   recently described (Badea et al., 2012). By varying registration parameters, the approach can be

377   used to identify the best set of parameters matching the results of manual parcellation. We varied

378   windows radius between 3 and 9 voxels, and gradient step for symmetric normalization between

379   0.10 and 2 voxels. The results of this analysis (Figure S3) show that the parameters choses (5 and

380   0.5 voxels, respectively) produce a good registration accuracy in all the brain regions tested.

381   These parameters are in agreement with those previously selected by Badea and colleagues using

382   *ex vivo* brain samples imaged at 9.4 Tesla.

383   Using these validated parameters, cross-strain volumetric analysis using anatomical

384   labels from the two atlases highlighted the presence of a general reduction in cortical volume in

385   BTBR mice with respect to B6 mice. Also major subcortical structures, including caudoputamen,

386   hippocampus and hypothalamus reported a statistical significant reduction in volume (Figure 7).

387   These results are in good agreement with recent comparative neuroanatomical mapping of these

388   two strains performed by other labs (Ellegood et al., 2013), where a similar significant decrease

389   in the volume of cortex and corpus callosum was shown.

390

391   *3.2. VBM*

392   Whole-brain VBM revealed widespread and bilateral reductions in GM volume across

393   dorsofrontal, cingulate, retrosplenial, occipital and parietal cortex (Figure 8, Z>3.1, p-

394   corrected<.001), in BTBR compared to B6 controls. These findings are in agreement with the

395   results of anatomical labelling. GM volume reductions were also evident in subcortical areas,

396   including the lateral and posterior thalamus (longitudinal fasciculus), the posterior hypothalamus

397   and the ventral hippocampus. Interestingly, VBM highlighted also small bilateral foci of

398   increased GM volume in the olfactory bulbs, in the medial pre-frontal and insular cortex, in the

399   amygdala and in the dorsal hippocampus. The detection of small focal effects that could not be

400   revealed when integrated over large anatomical volumes is one of the main advantages of the

401   VBM approach over classic neuroanatomical volumetric mapping. These results are in good

402   agreement with recent comparative neuroanatomical mapping of these two strains performed by

403 other labs using tensor based morphometry (Ellegood et al., 2013), which showed similar
404 significant alterations (using Tensor Based Morphometry, see discussion below) in hippocampal
405 and cortical areas.

406

407 *3.3. Cortical Thickness Estimation*

408   Further investigation of the presence of local alterations of GM in BTBR mice compared
409 to B6 controls was performed in terms of cortical thickness estimation. Average spatially-
410 normalized voxel-based thickness maps were calculated separately for each of the two strains
411 and three-dimensionally rendered for visualization purposes (Figure 9). In good agreement with
412 the results of automated anatomical labelling and VBM mapping, a widespread reduction in
413 mean cortical thickness ($Z>2.3$, p-corrected<0.01) was observed in BTBR mice compared to B6
414 controls. Importantly, inter-group voxel-wise statistics revealed significantly increased cortical
415 thickness in medial prefrontal and insular regions in the BTBR cohort ($Z>2.3$, p-corrected<0.01).

416

417 **4. Discussion and conclusions**

418   Here we described semi-automated procedures for automated anatomical labelling, VBM
419 and cortical thickness estimation in the mouse brain. The approach has been recently applied to
420 detect fine-grained morphoanatomical alterations in different mutant mouse lines, including
421 alterations in β-catenin mouse mutants (Tucci et al., 2014), acallosal and socially-impaired mice
422 (Dodero et al., 2013) and to identify sexually divergent effects on cortical anatomy in catechol-
423 O-methyltransferase mutant lines (Sannino et al., 2014). In the latter study, we showed
424 remarkably consistent intergroup differences in regional GM volume as assessed with our VBM
425 pipeline, or manual morphometric measurements of cortical thickness in post-mortem brain
426 slices (Sannino et al., 2014), thus underscoring the accuracy and sensitivity of our workflow.

427   The image processing described here adopts the methodologies and toolkits originally
428 developed for human brain imaging and can be straightforwardly extended to other areas of
429 research and mouse models of disease. For example, we also used VBM to describe symmetric
430 networks of anatomical covariance in the cortex of inbred mice complementary to those
431 previously identified in humans, providing a new tool to study gray matter disrupted connectivity
432 in brain disorders with transgenic mice (Pagani et al., 2016). Although prominent examples of
433 the use of morphoanatomical methods in the mouse have been recently described by other labs

434   (Badea et al., 2012; Borg and Chereul, 2008; Budin et al., 2013; Delatour et al., 2006; Johnson et

435   al., 2007; Lee et al., 2010; Lerch et al., 2011a; Nieman et al., 2005; Oguz and Sonka, 2014;

436   Sawiak et al., 2009; Sawiak et al., 2013), the vast majority of these contribution lack a detailed

437   description of the complex workflow required to process and analyse different

438   morphoanatomical readouts, thus complicating the replication of these methods by other groups.

439   The methodological workflow presented in this work was designed to facilitate the

440   implementation of fine-grained morphoanatomical mapping tools by non-expert users, and

441   promote forward and back translation of MRI preclinical and clinical research evidence. We also

442   point out that a preliminary account on the implementation of these procedures in parallel

443   computing cloud environment has been recently reported (Minervini et al., 2014), a strategy that

444   can streamline and accelerate image processing time by exploiting large high-performance-

445   computing infrastructures.

446   A dominant feature of our unified approach is the coupling of standard intensity based

447   affine registration with a symmetric diffeomorphic normalization algorithm to obtain optimal

448   MR image registration (Avants et al., 2008). This approach, which has been successfully

449   employed both in human (Kim et al., 2008; Klein et al., 2009; Klein et al., 2010) and small

450   animal imaging studies (Avants et al., 2010b; Lerch et al., 2011b), is based on the ANTs open

451   source software library and is adopted to create a study based template, carry out skull stripping

452   and perform anatomical labelling via label propagation. Our cortical thickness estimation

453   approach is also registration-based, and employs *DiReCT*, an advanced diffeomorphic

454   registration algorithm implemented in ANTs toolkit that has been recently validated on human

455   imaging data (Das et al., 2009) and used for research studies with clinical population (Avants et

456   al., 2010a). To the best of our knowledge, this is the first example of the application of this

457   approach to map cortical thickness in small rodent species.

458   The cortical thickness mapping and anatomical labelling approaches employed rely on

459   the availability of three dimensional labelled MRI atlases with delineated cortical and subcortical

460   morphology. While a universally accepted MRI atlas of the mouse brain is still not available, a

461   number of mouse brain MRI atlases have been published based on high resolution acquisitions of

462   a single subject (Badea et al., 2012; Maheswaran et al., 2009a; Xie et al., 2010; Zhang et al.,

463   2010) or constructed from several animals, with data gathered either *in vivo* (Aggarwal et al.,

464   2009; Ma et al., 2008; Maheswaran et al., 2009b) or from *ex vivo* fixed specimens (Aggarwal et

465 al., 2009; Badea et al., 2007; Dorr et al., 2008; Johnson et al., 2010; Kovacevic et al., 2005;

466 Ullmann et al., 2013). In this study, a combination of two atlases was employed to obtain a fine-

467 grained parcellation of both cortical (Ullmann et al., 2013) and subcortical (Dorr et al., 2008;

468 Ullmann et al., 2013) regions. However, our method is not atlas-dependent and can be flexibly

469 adapted to a number of published or custom mouse brain MRI anatomical partitions.

470   An important benefit of our approach is the possibility to measure different and

471 complementary morphoanatomical brain metrics - including volumetric analysis, VBM and

472 cortical thickness - in a single reference space. This aspect is of crucial importance, as it

473 broadens the scope of application of MRI-based brain morphometry and it augments its

474 translational potential by permitting a multi parametric comparison with analogous clinical

475 readouts. In the illustrative example reported here, an overall agreement between the three

476 readouts was found. Apparent discrepancies between readouts (e.g., the lack of inter-strain

477 differences in insular volume, due to the presence of VBM foci of increased and decreased

478 regional volume in anterior and posterior portions of this region) are the result of different

479 sampling scales (label vs. voxel level) of the readouts employed. We also note that the

480 combination of complementary approaches can help disambiguate morphological alterations of

481 pathological origin, as the relationship between thickness and local GM volume has not been

482 thoroughly clarified, and may probably change across pathologies and populations (Hutton et al.,

483 2008). Within this scenario, the use of complementary metrics coupled to histological staining

484 can help to pinpoint the pathological bases of brain morphometric changes of neuropathological

485 origin.

486   In addition, our preprocessing workflow can be straightforwardly extended to perform

487 tensor based morphometry (TBM). As in VBM, TBM entails the local computation of the

488 Jacobian determinants of the deformation field used to map subjects' images to the study based

489 template. The Jacobian determinant (i.e. the local scaling factor) encodes for local anatomical

490 expansions and contractions of subjects' areas relative to the study based template, and therefore

491 Jacobian maps can be used to localise inter-group differences in the local shape of brain

492 structures at the voxel level. TBM analysis can be simply performed by omitting the tissue

493 segmentation step in the VBM procedure herein described. As TBM does not entail tissue

494 classification, it can be used for the simultaneous investigation of WM and GM alterations, and

495 may robustly detect alterations in areas of mixed WM-GM structures, such as the thalamus and

16

496 brain stem, which are especially sensitive to the accuracy of intensity based tissue classification
497 algorithms.

498   A few methodological limitations in our approach deserved to be mentioned. The
499 procedure described here has been developed and optimized or fixed *ex vivo* brain samples
500 imaged at 7 Tesla using T2-weighted images. While the application of our workflow to different
501 field strengths and image contrast is conceivable, adjustments in single preprocessing parameters
502 may be required to adapt our procedure to different contrast mechanisms or images acquired at
503 different field strengths. One limitation of our cortical thickness mapping is its poor performance
504 in resolving thickness at the level of inter-hemispheric fissure in medial regions of the mouse
505 cortex such as cingulate or retrosplenial areas (Figure S2). As a result, inter-group differences in
506 cortical thickness in these regions should be interpreted with caution. Researchers interested in
507 mapping gray matter alterations in these regions with high confidence, should consider cross
508 validating thickness mapping with voxelwise methods described in our workflow that are
509 immune to this limitation, such as VBM and TBM. Similarly, the segmentation of the anterior
510 cingulate in acallosal mice such as BTBR should be considered tentative, as the lack of clear
511 white matter gray matter boundary prevents an empirical assessment of its accuracy. Once again,
512 voxelwise-based morphoanatomical mapping together with histological measurements can help
513 validate cortical thickness measurements in these areas when acallosal mice are employed.
514 Caution should also be exercised in interpreting inter-group differences in mouse models
515 characterized by profound demyelination and neurodegeneration, two conditions that can reduce
516 GM/WM contrast and affect segmentation accuracy for VBM. Notwithstanding these limitations,
517 the possibility of using a unified workflow to map multiple complementary morphoanatomical
518 parameters should be emphasized as a major point of strength of our approach, owing to the
519 possibility of cross-comparing different readouts to dissect specific neuroanatomical features
520 with increased confidence.

521   In conclusion, we described a registration-based approach for anatomical mapping, VBM
522 and cortical thickness estimation in the mouse brain. The application of these procedures enabled
523 the identification of subtle volumetric differences across subjects without prior knowledge of
524 structures of interest. Our unified approach based on diffeomorphic registration permits to
525 integrate complementary MR morphoanatomical techniques, and is based on popular open
526 source software (ANTs), which has been extensively employed in priori MRI morphometric

527   studies. The detailed operational workflow described in the present work is expected to help the

528   implementation of rodent morphoanatomical methods by non-expert users, thus ultimately

529   promoting the use of these tools across the preclinical neuroimaging community.

530

Captions

Figure 1. Preprocessing workflow.

Each MRI subject image undergoes a first correction for intensity non-uniformity bias using the *N3BiasFieldCorrection*. To create individual subject masks, a masked representative reference subject is registered to each subject, and the transformation of this registration is then applied to the reference subject mask. The application of this mask permits to remove most extra brain tissue. Non-uniformity bias is subsequently estimated for individual masked brains. The preprocessing procedure outputs a skull-stripped bias-corrected image and a companion binary brain mask for each subject.

Figure 2. Preprocessing results.

In this illustrative example, the original subject image (a) is bias corrected before (b) and after (e) skull stripping (d). Note the improved bias field correction after skull stripping (f) with respect to the bias correction prior skull stripping (c), especially in the ventral part of the brain and in the ventricles. Voxels intensity is represented in shades of red to magnify image contrast.

Figure 3. Automated anatomical labelling and cortical thickness estimation.

Upper box: Anatomical labels of the MRI atlas are registered into each subject space via the study based template through a combination of linear and diffeomorphic mapping, using *antsRegistration* and *WarpImageMultiTransform*. A propagation of the labels from the MRI atlas to each subject space is then performed via the study based template, followed by the estimation of the volume for each label. Lower box: Anatomical labels of the cortical mantle in the subject space are merged together to build a unified cortical label. This cortical label and subject brain mask of the subjects are used to create the inputs needed to estimate the cortical thickness using *DiReCT*. The obtained cortical thickness maps are eventually warped again into the study based space and smoothed for subsequent statistical comparison.

Figure 4. VBM.

Each preprocessed subject image is mapped on the study based template space through a combination of linear and diffeomorphic mapping, using *antsRegistration* and *WarpImageMultiTransform*. Registered volumes are segmented using the study based template priors. Grey matter probability maps for each subject are then modulated using Jacobian maps obtained from the registration process and smoothed for subsequent statistical comparison.

Figure 5. Study based template and tissue segmentation.

Orthogonal slice view of a study based template of the B6 mice population obtained using the iterative diffeomorphic registration process of the *buildtemplateparallel* script and its corresponding tissue segmentation (a). The template is segmented using *Atropos* in 6 different tissue classes which are used as a-priori information for individual estimation of gray matter in VBM. The different tissue classes of the template are combined to obtain gray matter (b) and non gray matter components (c, white matter, plus ventricular regions and CSF).

569   **Figure 6. Correlation plot between *DiReCT* outputs and manual measurements of cortical thickness.**

570   Secondary motor (M2), secondary somatosensory (S2) and auditory cortex (Au) were chosen as representative

571   cortical areas to validate our cortical thickness methodology. Representative measures from DiReCT and manual

572   estimates are reported for selected cortical regions (middle panel). A correlation plot of manual and automatic

573   measurements highlighted an excellent correspondence between the twee readouts in terms of Pearson's correlation

574   (r=0.99; p<0.001).

575

576   **Figure 7. Anatomical labelling.**

577   The labels of the reference atlas employed are warped into subjects' space via the study based template using the

578   combination of affine and diffeomorphic mapping obtained after the registration process. The registered labels

579   permit to calculate volumes of brain areas of interest and perform t-tests between the mouse samples. (Cpu:

580   caudoputamen; Th: thalamus; OB: olfactory bulbs; HP: hippocampus; Hyp: hypothalamus, CC: corpus callosum;

581   OF: orbitofrontal cortex; RS: retrosplenial cortex; M1: primary motor cortex; V1: primary visual cortex; Rh: rhinal

582   cortex). **p<.01; ***p<.001.)

583

584   **Figure 8. VBM.**

585   Differences in local gray matter volumes are assessed combining gray matter probability maps and local Jacobian

586   determinants. Statistical comparison (p<.01, threshold-free cluster enhancement followed by cluster-based

587   thresholding) showed widespread and bilateral reductions in grey matter volumes across dorsofrontal, cingulate,

588   retrosplenial, occipital and parietal cortex as well as in subcortical structures in BTBR compared to B6 controls.

589   VBM highlighted also small bilateral foci of increased gray matter volume in the olfactory bulbs, in the medial pre-

590   frontal and insular cortex, in the amygdala and in the dorsal hippocampus. (Cb: cerebellum; Cpu: caudoputamen;

591   DHyp: dorsal hypothalamus; dPFC: dorsal prefrontal cortex; LTh: lateral thalamus; mPFC: medial prefrontal

592   cortex; OB: olfactory bulbs; Rh: rhinal cortex; RS: retrosplenial cortex).

593

594   **Figure 9. Cortical thickness estimation.**

595   Three-dimensional rendering views of average cortical thickness in BTBR and B6 mice (a). Statistical comparison

596   showed significant cortical thickness thinning (p<0.01, threshold-free cluster enhancement followed by cluster-

597   based thresholding) in parietal, temporal and peri-hippocampal cortex of BTBR mice. Increased thickness was

598   observed in medial prefrontal and anterior insular regions of this strain (b).

599

600   **Figure S1. Segmentation of the study based template using six tissue classes provides accurate GM/WM**

601   **separation.**

602   A: Standard three-class segmentation of our ex vivo brains using Atropos did not produce an accurate GM/WM

603   separation, with a great overestimation of white matter fraction. Anatomical template (left), plus the segmentation

604   classes obtained with a three-cluster segmentation approach (WM, mixed WM/GM and GM matter maps, from left

605   to right, respectively). B: The combined use of six independent segmentation classes leads to a more accurate

606   separation of GM and WM. The final GM map is the combined result of three GM classes (middle row). Additional
607   non-GM tissue can be obtained by merging the remaining three classes.
608
609   **Figure S2. Cortical thickness estimation.**
610   In lissencephalic brains, DiReCT measurement results in a string of voxels exhibiting constant thickness. This
611   appears in the form of parallel cortical "columns" in coronal brain slices clearly visible in the magnified view, where
612   colors represent the norm of the deformation field that is the estimated thickness.
613
614   **Figure S3. Optimization of registration parameters for anatomical labelling.**
615   Accuracy of registration (Dice coefficient) for varying registration parameters (window radius for cross correlation
616   and gradient steps). Top: as in Badea et al., (2012), we varied windows radius between 3 and 9 voxels. The chosen
617   value (5 voxels) produces a good performance in all the brain regions tested. Bottom: the gradient step parameter for
618   the symmetric normalization was varied between 0.10 and 2 voxels. The chosen parameter (0.5 voxels) produces a
619   good performance in all the tested regions.

References

Aggarwal M, Zhang J, Miller MI, Sidman RL, Mori S. Magnetic resonance imaging and micro-computed tomography combined atlas of developing and adult mouse brains for stereotaxic surgery. Neuroscience, 2009; 162: 1339-50.

Ashburner J, Friston KJ. Voxel-based morphometry--the methods. Neuroimage, 2000; 11: 805-21.

Avants BB, Cook PA, Ungar L, Gee JC, Grossman M. Dementia induces correlated reductions in white matter integrity and cortical thickness: a multivariate neuroimaging study with sparse canonical correlation analysis. Neuroimage, 2010a; 50: 1004-16.

Avants BB, Epstein CL, Grossman M, Gee JC. Symmetric diffeomorphic image registration with cross-correlation: Evaluating automated labeling of elderly and neurodegenerative brain. Medical Image Analysis, 2008; 12: 26-41.

Avants BB, Tustison N, Song G. Advanced normalization tools (ANTS). Insight J, 2009.

Avants BB, Tustison NJ, Stauffer M, Song G, Wu B, Gee JC. The Insight ToolKit image registration framework. Frontiers in neuroinformatics, 2014; 8.

Avants BB, Tustison NJ, Wu J, Cook PA, Gee JC. An open source multivariate framework for n-tissue segmentation with evaluation on public data. Neuroinformatics, 2011; 9: 381-400.

Avants BB, Yushkevich P, Pluta J, Minkoff D, Korczykowski M, Detre J, Gee JC. The optimal template effect in hippocampus studies of diseased populations. Neuroimage, 2010b; 49: 2457-66.

Badea A, Ali-Sharief AA, Johnson GA. Morphometric analysis of the C57BL/6J mouse brain. Neuroimage, 2007; 37: 683-93.

Badea A, Gewalt S, Avants BB, Cook JJ, Johnson GA. Quantitative mouse brain phenotyping based on single and multispectral MR protocols. Neuroimage, 2012; 63: 1633-45.

Borg J, Chereul E. Differential MRI patterns of brain atrophy in double or single transgenic mice for APP and/or SOD. J Neurosci Res, 2008; 86: 3275-84.

Budin F, Hoogstoel M, Reynolds P, Grauer M, O'Leary-Moore SK, Oguz I. Fully automated rodent brain MR image processing pipeline on a Midas server: from acquired images to region-based statistics. Front Neuroinform, 2013; 7: 15.

Cahill LS, Laliberté CL, Ellegood J, Spring S, Gleave JA, van Eede MC, Lerch JP, Henkelman RM. Preparation of fixed mouse brains for MRI. Neuroimage, 2012; 60: 933-9.

Chou C-H, Su M-C, Lai E. A new cluster validity measure and its application to image compression. Pattern Analysis and Applications, 2004; 7: 205-20.

Cutuli D, Pagani M, Caporali P, Galbusera A, Laricchiuta D, Foti F, Neri C, Spalletta G, Caltagirone C, Petrosini L. Effects of Omega-3 Fatty Acid Supplementation on Cognitive Functions and Neural Substrates: A Voxel-Based Morphometry Study in Aged Mice. Frontiers in aging neuroscience, 2016; 8.

Das SR, Avants BB, Grossman M, Gee JC. Registration based cortical thickness measurement. Neuroimage, 2009; 45: 867-79.

Delatour B, Guegan M, Volk A, Dhenain M. In vivo MRI and histological evaluation of brain atrophy in APP/PS1 transgenic mice. Neurobiol Aging, 2006; 27: 835-47.

Dice LR. Measures of the amount of ecologic association between species. Ecology, 1945; 26: 297-302.

Dodero L, Damiano M, Galbusera A, Bifone A, Tsaftsaris SA, Scattoni ML, Gozzi A. Neuroimaging evidence of major morpho-anatomical and functional abnormalities in the BTBR T+TF/J mouse model of autism. PLoS One, 2013; 8.

Dorr AE, Lerch JP, Spring S, Kabani N, Henkelman RM. High resolution three-dimensional brain atlas using an average magnetic resonance image of 40 adult C57Bl/6J mice. Neuroimage, 2008; 42: 60-9.

670   Ellegood J, Babineau BA, Henkelman RM, Lerch JP, Crawley JN. Neuroanatomical analysis of
671   the BTBR mouse model of autism using magnetic resonance imaging and diffusion tensor
672   imaging. Neuroimage, 2013; 70: 288-300.
673   Friston KJ, Holmes AP, Worsley KJ, Poline JP, Frith CD, Frackowiak RS. Statistical parametric
674   maps in functional imaging: a general linear approach. Human brain mapping, 1994; 2: 189-
675   210.
676   Hutton C, De Vita E, Ashburner J, Deichmann R, Turner R. Voxel-based cortical thickness
677   measurements in MRI. Neuroimage, 2008; 40: 1701-10.
678   Jenkinson M, Beckmann CF, Behrens TE, Woolrich MW, Smith SM. Fsl. Neuroimage, 2012; 62:
679   782-90.
680   Jia H, Yap PT, Wu G, Wang Q, Shen D. Intermediate templates guided groupwise registration
681   of diffusion tensor images. Neuroimage, 2011; 54: 928-39.
682   Johnson GA, Ali-Sharief A, Badea A, Brandenburg J, Cofer G, Fubara B, Gewalt S, Hedlund
683   LW, Upchurch L. High-throughput morphologic phenotyping of the mouse brain with magnetic
684   resonance histology. Neuroimage, 2007; 37: 82-9.
685   Johnson GA, Badea A, Brandenburg J, Cofer G, Fubara B, Liu S, Nissanov J. Waxholm space:
686   an image-based reference for coordinating mouse brain research. Neuroimage, 2010; 53:
687   365-72.
688   Kim J, Avants B, Patel S, Whyte J, Coslett BH, Pluta J, Detre JA, Gee JC. Structural
689   consequences of diffuse traumatic brain injury: a large deformation tensor-based
690   morphometry study. Neuroimage, 2008; 39: 1014-26.
691   Klein A, Andersson J, Ardekani BA, Ashburner J, Avants B, Chiang M-C, Christensen GE,
692   Collins DL, Gee J, Hellier P. Evaluation of 14 nonlinear deformation algorithms applied to
693   human brain MRI registration. Neuroimage, 2009; 46: 786-802.
694   Klein A, Ghosh SS, Avants B, Yeo BT, Fischl B, Ardekani B, Gee JC, Mann JJ, Parsey RV.
695   Evaluation of volume-based and surface-based brain image registration methods.
696   Neuroimage, 2010; 51: 214-20.
697   Kovacevic N, Henderson JT, Chan E, Lifshitz N, Bishop J, Evans AC, Henkelman RM, Chen XJ.
698   A three-dimensional MRI atlas of the mouse brain with estimates of the average and
699   variability. Cereb Cortex, 2005; 15: 639-45.
700   Lassi G, Priano L, Maggi S, Garcia-Garcia C, Balzani E, El-Assawy N, Pagani M, Tinarelli F,
701   Giardino D, Mauro A. Deletion of the Snord116/SNORD116 Alters Sleep in Mice and Patients
702   with Prader-Willi Syndrome. Sleep, 2015.
703   Lee D, Ruffins S, Ng Q, Sane N, Anderson S, Toga A. MBAT: a scalable informatics system for
704   unifying digital atlasing workflows. BMC Bioinformatics, 2010; 11: 1471-2105.
705   Lee J, Ehlers C, Crews F, Niethammer M, Budin F, Paniagua B, Sulik K, Johns J, Styner M,
706   Oguz I. Automatic cortical thickness analysis on rodent brain. Proc Soc Photo Opt Instrum
707   Eng, 2011; 15: 7962481-79624811.
708   Lerch JP, Carroll JB, Dorr A, Spring S, Evans AC, Hayden MR, Sled JG, Henkelman RM.
709   Cortical thickness measured from MRI in the YAC128 mouse model of Huntington's disease.
710   Neuroimage, 2008; 41: 243-51.
711   Lerch JP, Gazdzinski L, Germann J, Sled JG, Henkelman RM, Nieman BJ. Wanted dead or
712   alive? The tradeoff between in-vivo versus ex-vivo MR brain imaging in the mouse. Front
713   Neuroinform, 2012; 6: 6.
714   Lerch JP, Sled JG, Henkelman RM. MRI phenotyping of genetically altered mice. Magnetic
715   Resonance Neuroimaging. Springer, 2011a: 349-61.
716   Lerch JP, Yiu AP, Martinez-Canabal A, Pekar T, Bohbot VD, Frankland PW, Henkelman RM,
717   Josselyn SA, Sled JG. Maze training in mice induces MRI-detectable brain shape changes
718   specific to the type of learning. Neuroimage, 2011b; 54: 2086-95.
719   Li Q, Cheung C, Wei R, Hui ES, Feldon J, Meyer U, Chung S, Chua SE, Sham PC, Wu EX.
720   Prenatal immune challenge is an environmental risk factor for brain and behavior change

721 relevant to schizophrenia: evidence from MRI in a mouse model. PLoS One, 2009; 4: e6354.
722 Ma Y, Smith D, Hof PR, Foerster B, Hamilton S, Blackband SJ, Yu M, Benveniste H. In Vivo 3D
723 Digital Atlas Database of the Adult C57BL/6J Mouse Brain by Magnetic Resonance
724 Microscopy. Front Neuroanat, 2008; 2.
725 Maheswaran S, Barjat H, Bate ST, Aljabar P, Hill DL, Tilling L, Upton N, James MF, Hajnal JV,
726 Rueckert D. Analysis of serial magnetic resonance images of mouse brains using image
727 registration. Neuroimage, 2009a; 44: 692-700.
728 Maheswaran S, Barjat H, Rueckert D, Bate ST, Howlett DR, Tilling L, Smart SC, Pohlmann A,
729 Richardson JC, Hartkens T, Hill DL, Upton N, Hajnal JV, James MF. Longitudinal regional
730 brain volume changes quantified in normal aging and Alzheimer's APP x PS1 mice using
731 MRI. Brain Res, 2009b; 13: 19-32.
732 Minervini M, Rusu C, Damiano M, Tucci V, Bifone A, Gozzi A, Tsaftaris SA. Large-scale
733 analysis of neuroimaging data on commercial clouds with content-aware resource allocation
734 strategies. International Journal of High Performance Computing Applications, 2014:
735 1094342013519483.
736 Mueller S, Keeser D, Reiser MF, Teipel S, Meindl T. Functional and structural MR imaging in
737 neuropsychiatric disorders, part 2: application in schizophrenia and autism. AJNR Am J
738 Neuroradiol, 2012; 33: 2033-7.
739 Nestler EJ, Hyman SE. Animal models of neuropsychiatric disorders. Nat Neurosci, 2010; 13:
740 1161-9.
741 Nieman BJ, Bock NA, Bishop J, Chen XJ, Sled JG, Rossant J, Henkelman RM. Magnetic
742 resonance imaging for detection and analysis of mouse phenotypes. NMR Biomed, 2005; 18:
743 447-68.
744 Oguz I, Sonka M. LOGISMOS-B: layered optimal graph image segmentation of multiple objects
745 and surfaces for the brain. IEEE Trans Med Imaging, 2014; 33: 1220-35.
746 Pagani M, Bifone A, Gozzi A. Structural covariance networks in the mouse brain. Neuroimage,
747 2016.
748 Sannino S, Gozzi A, Cerasa A, Piras F, Scheggia D, Manago F, Damiano M, Galbusera A,
749 Erickson LC, De Pietri Tonelli D, Bifone A, Tsaftaris SA, Caltagirone C, Weinberger DR,
750 Spalletta G, Papaleo F. COMT Genetic Reduction Produces Sexually Divergent Effects on
751 Cortical Anatomy and Working Memory in Mice and Humans. Cereb Cortex, 2014; 21: 21.
752 Sawiak S, Wood N, Williams G, Morton A, Carpenter T. SPMMouse: A new toolbox for SPM in
753 the animal brain. ISMRM 17th Scientific Meeting & Exhibition, April, 2009: 18-24.
754 Sawiak SJ, Wood NI, Williams GB, Morton AJ, Carpenter TA. Voxel-based morphometry with
755 templates and validation in a mouse model of Huntington's disease. Magnetic Resonance
756 Imaging, 2013; 31: 1522-31.
757 Sforazzini F, Bertero A, Dodero L, David G, Galbusera A, Scattoni ML, Pasqualetti M, Gozzi A.
758 Altered functional connectivity networks in acallosal and socially impaired BTBR mice. Brain
759 Structure and Function, 2014a: 1-14.
760 Sforazzini F, Schwarz AJ, Galbusera A, Bifone A, Gozzi A. Distributed BOLD and CBV-
761 weighted resting-state networks in the mouse brain. Neuroimage, 2014b; 87: 403-15.
762 Squillace M, Dodero L, Federici M, Migliarini S, Errico F, Napolitano F, Krashia P, Di Maio A,
763 Galbusera A, Bifone A, Scattoni ML, Pasqualetti M, Mercuri NB, Usiello A, Gozzi A.
764 Dysfunctional dopaminergic neurotransmission in asocial BTBR mice. Transl Psychiatry,
765 2014; 4: e427.
766 Tucci V, Kleefstra T, Hardy A, Heise I, Maggi S, Willemsen MH, Hilton H, Esapa C, Simon M,
767 Buenavista MT, McGuffin LJ, Vizor L, Dodero L, Tsaftaris S, Romero R, Nillesen WN, Vissers
768 LE, Kempers MJ, Vulto-van Silfhout AT, Iqbal Z, Orlando M, Maccione A, Lassi G, Farisello P,
769 Contestabile A, Tinarelli F, Nieus T, Raimondi A, Greco B, Cantatore D, Gasparini L,
770 Berdondini L, Bifone A, Gozzi A, Wells S, Nolan PM. Dominant beta-catenin mutations cause
771 intellectual disability with recognizable syndromic features. J Clin Invest, 2014; 124: 1468-82.

772 Ullmann JF, Watson C, Janke AL, Kurniawan ND, Reutens DC. A segmentation protocol and
773   MRI atlas of the C57BL/6J mouse neocortex. Neuroimage, 2013; 78: 196-203.
774 Worsley KJ, Evans AC, Marrett S, Neelin P. A three-dimensional statistical analysis for CBF
775   activation studies in human brain. Journal of Cerebral Blood Flow and Metabolism, 1992; 12:
776   900-.
777 Wu K-L, Yang M-S. A cluster validity index for fuzzy clustering. Pattern Recognition Letters,
778   2005; 26: 1275-91.
779 Xie Z, Yang D, Stephenson D, Morton D, Hicks C, Brown T, Bocan T. Characterizing the
780   regional structural difference of the brain between tau transgenic (rTg4510) and wild-type
781   mice using MRI. Med Image Comput Comput Assist Interv, 2010; 13: 308-15.
782 Yushkevich PA, Piven J, Hazlett HC, Smith RG, Ho S, Gee JC, Gerig G. User-guided 3D active
783   contour segmentation of anatomical structures: significantly improved efficiency and reliability.
784   Neuroimage, 2006; 31: 1116-28.
785 Zhang J, Peng Q, Li Q, Jahanshad N, Hou Z, Jiang M, Masuda N, Langbehn DR, Miller MI, Mori
786   S, Ross CA, Duan W. Longitudinal characterization of brain atrophy of a Huntington's disease
787   mouse model by automated morphological analyses of magnetic resonance images.
788   Neuroimage, 2010; 49: 2340-51.
789
790
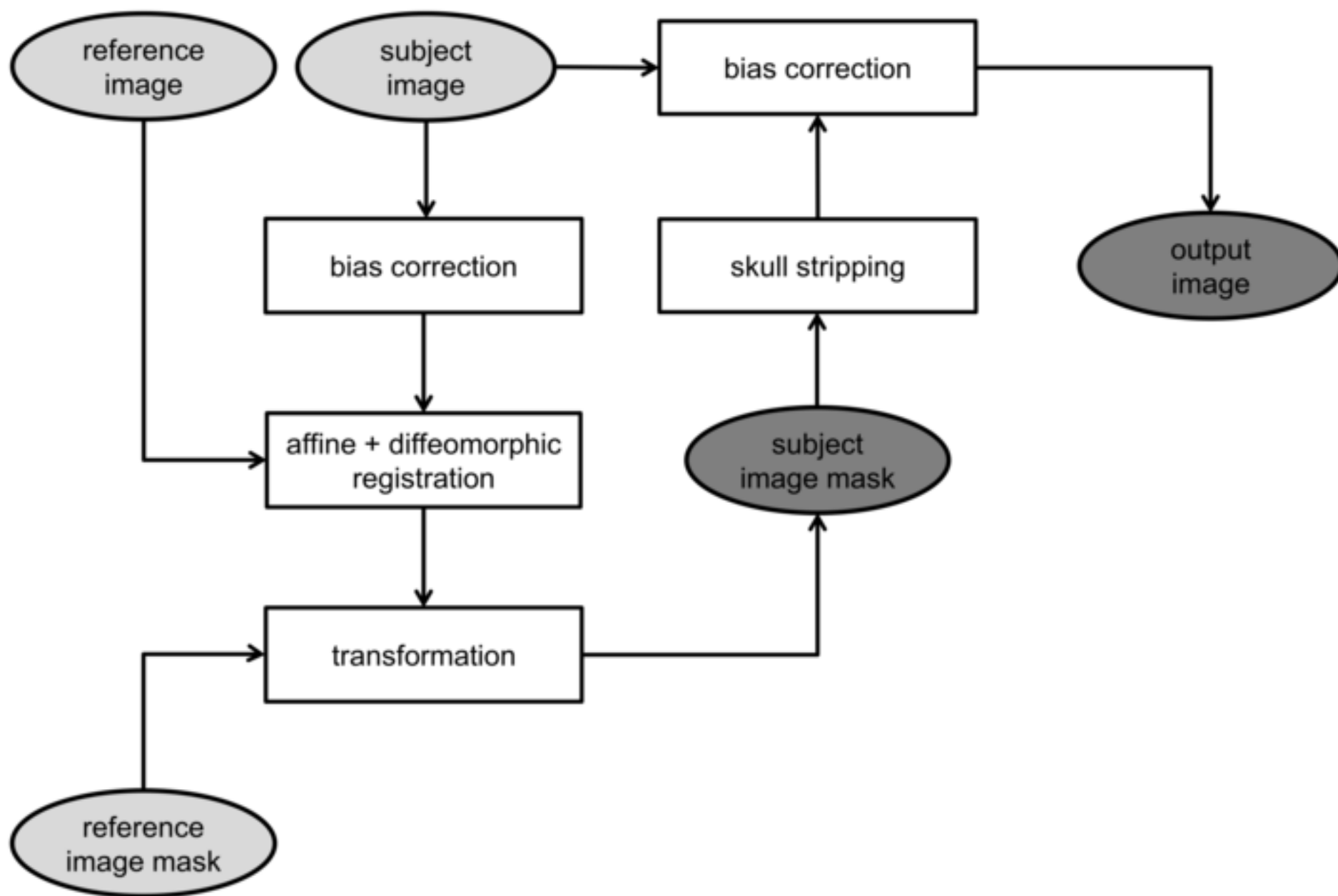
a) subject image

b) bias field

c) bias correction

d) subject image mask

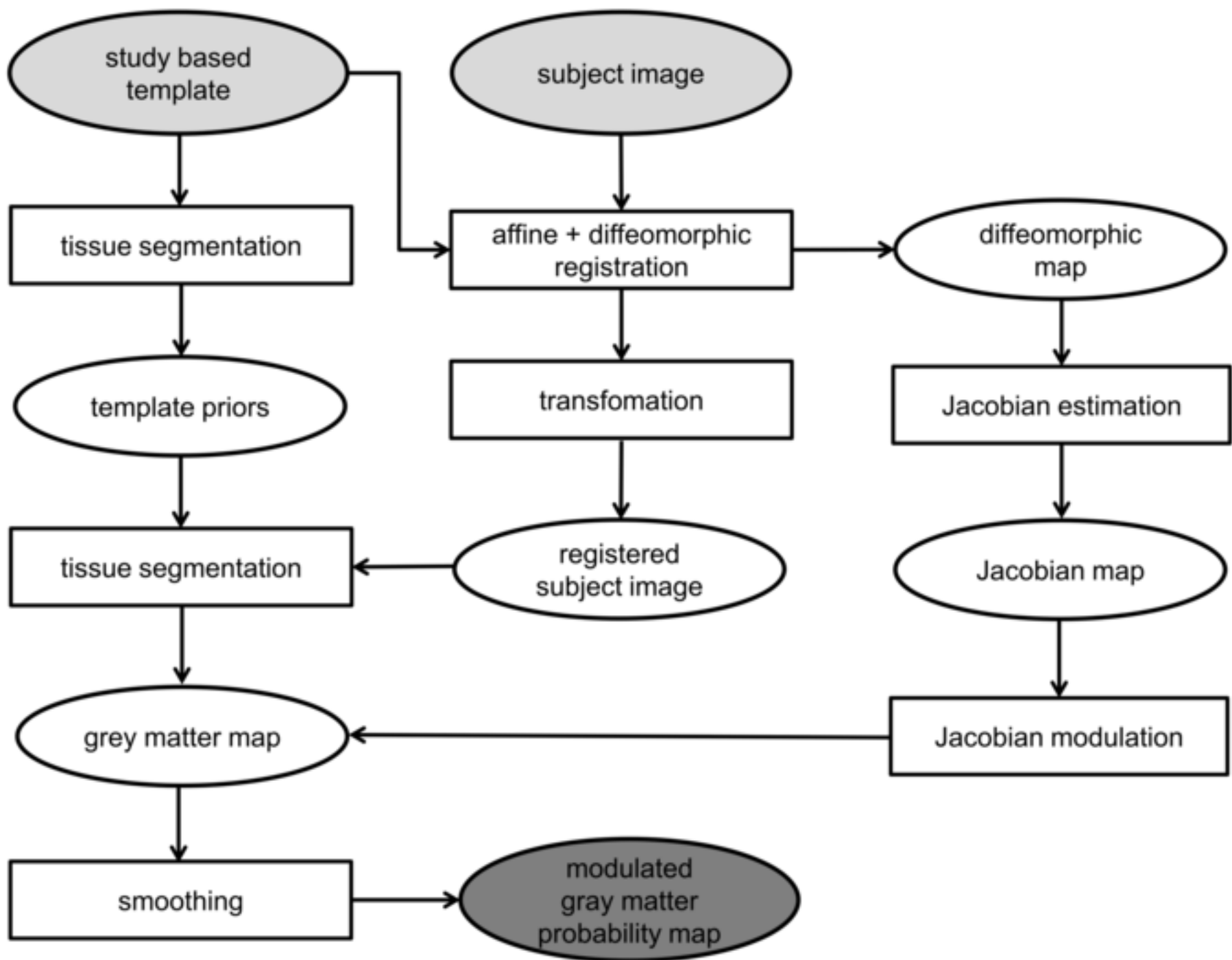e) bias field
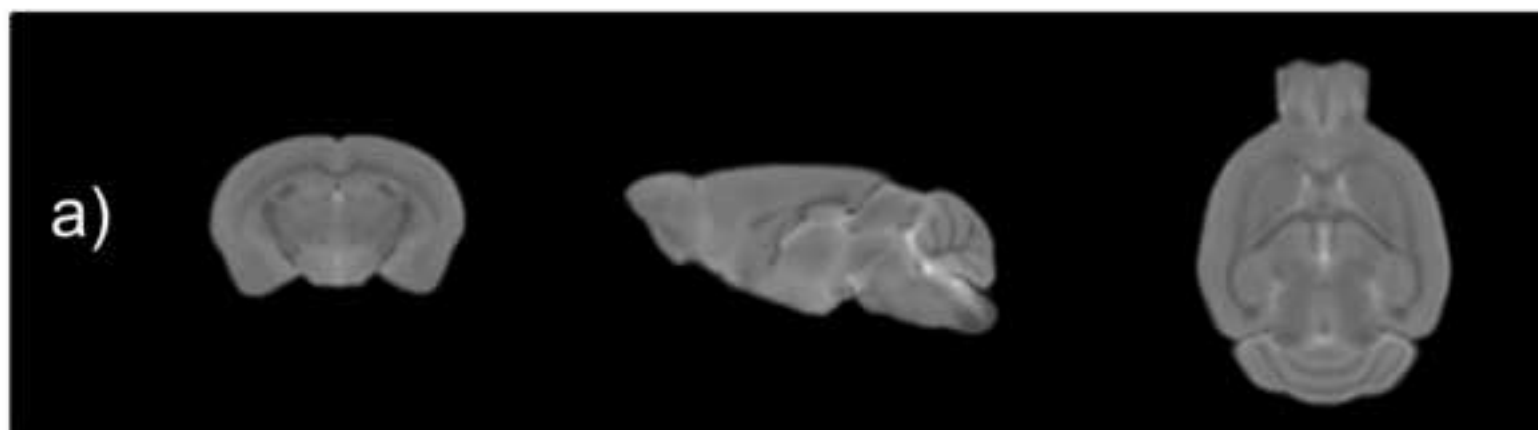
f) bias correction after skull stripping
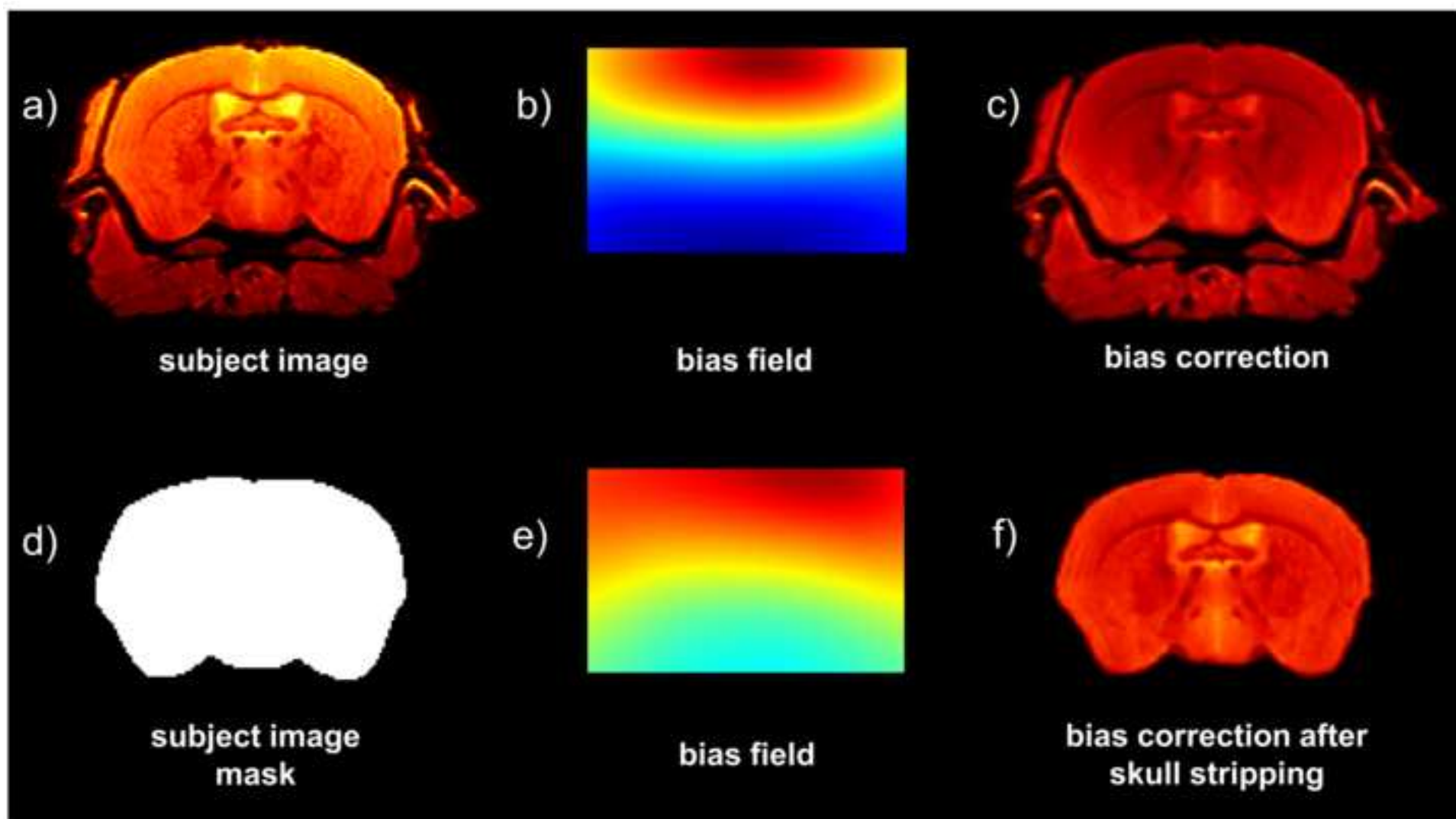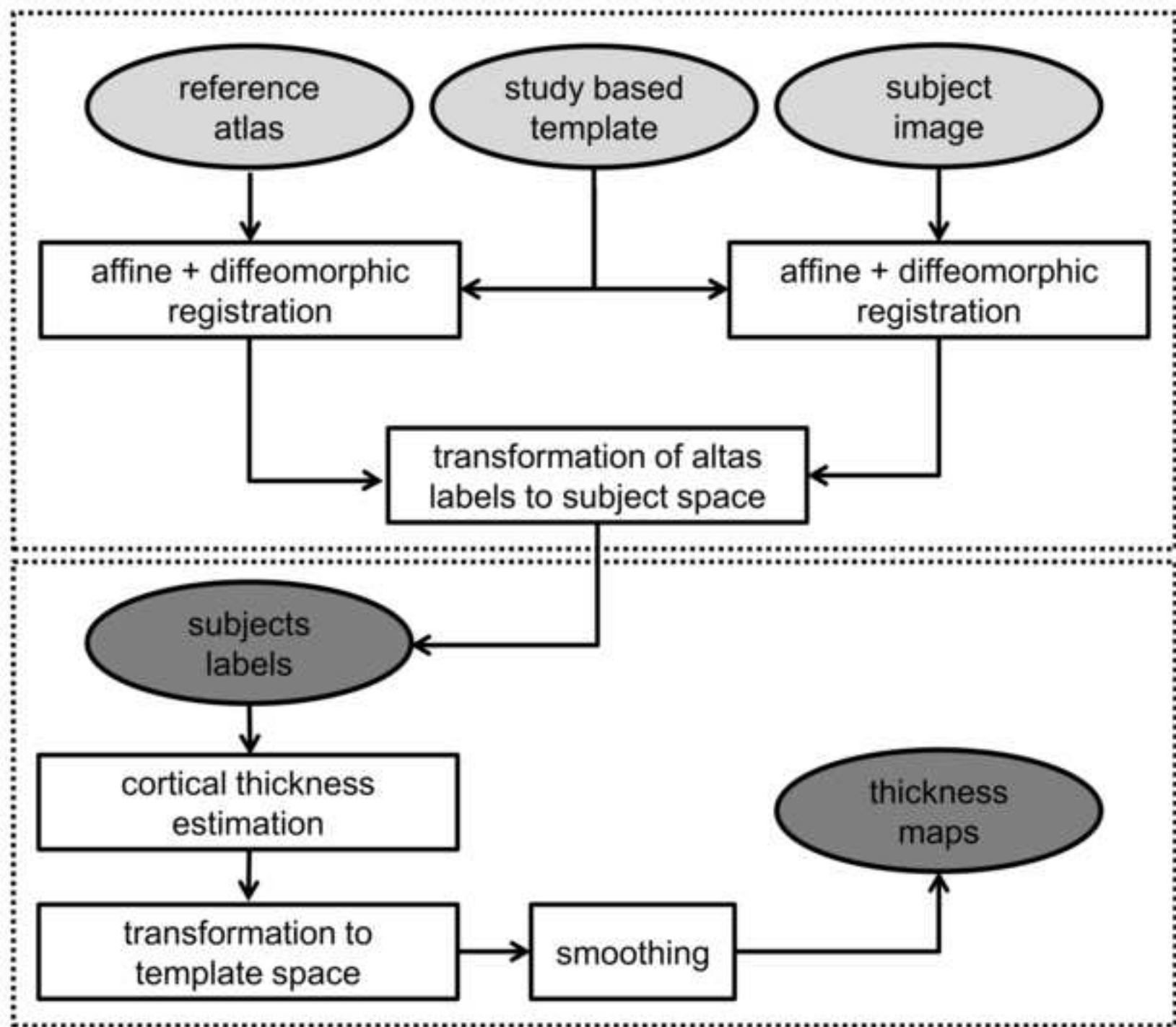
Figure 4
[Click here to download high resolution image](#)

Figure 5
Click here to download high resolution image

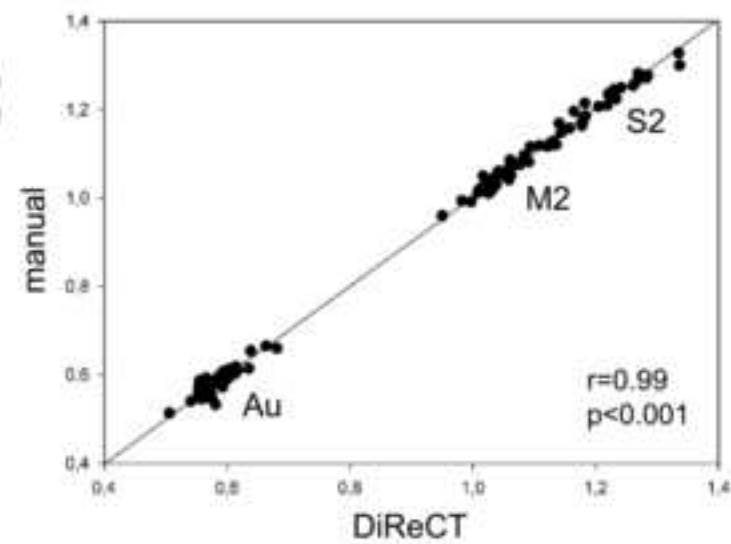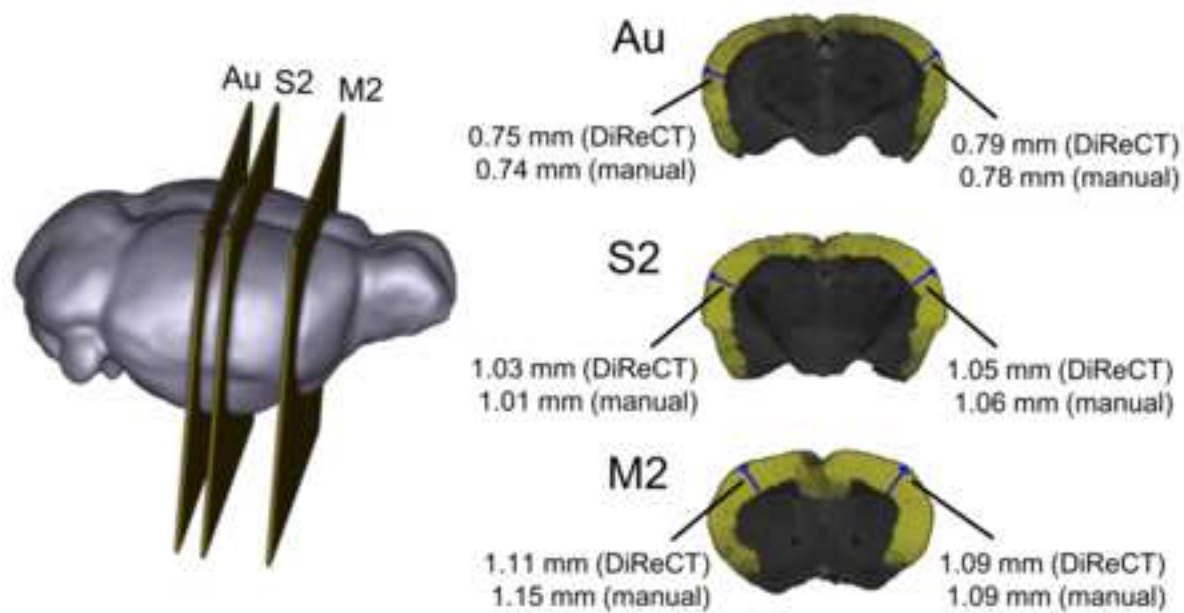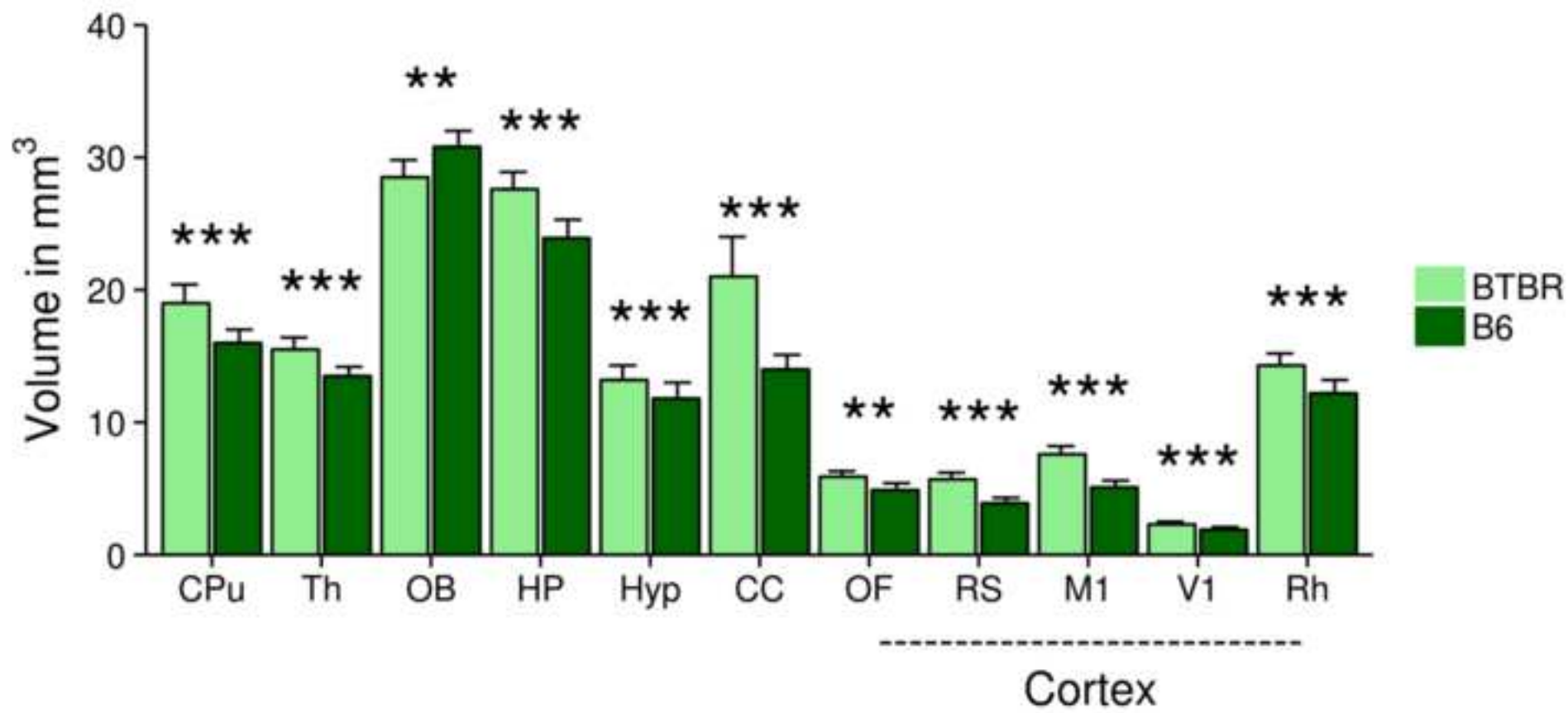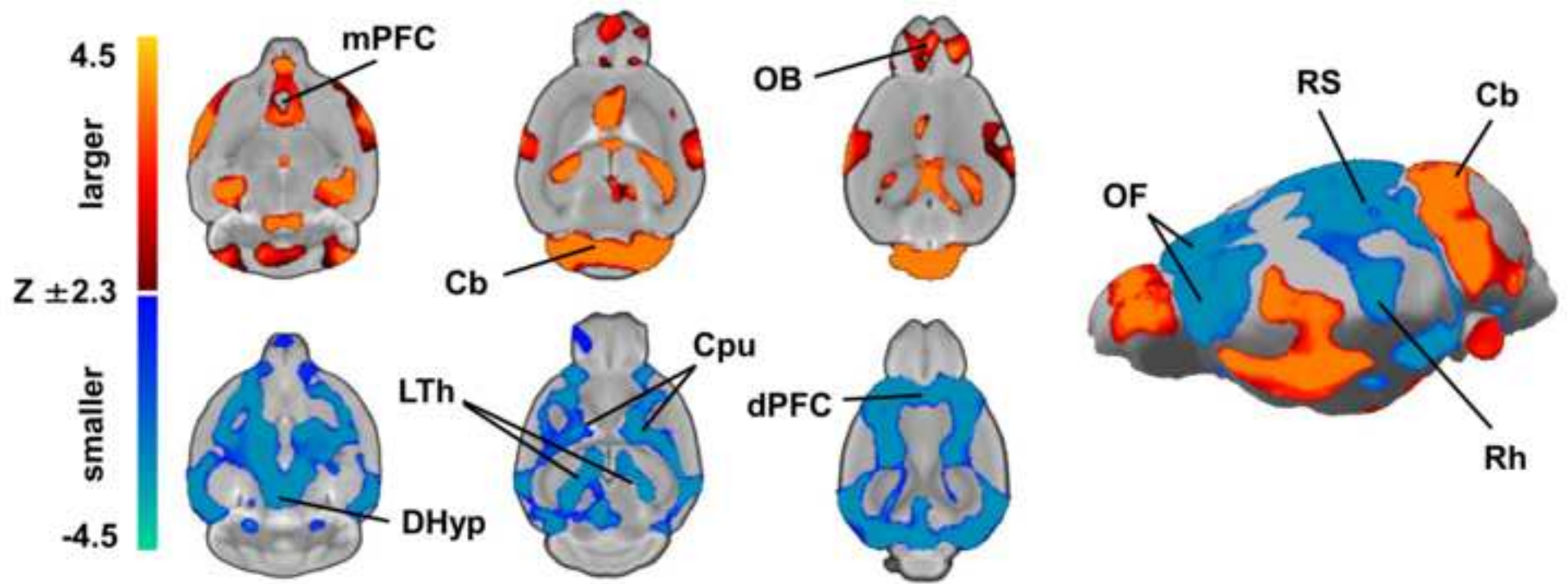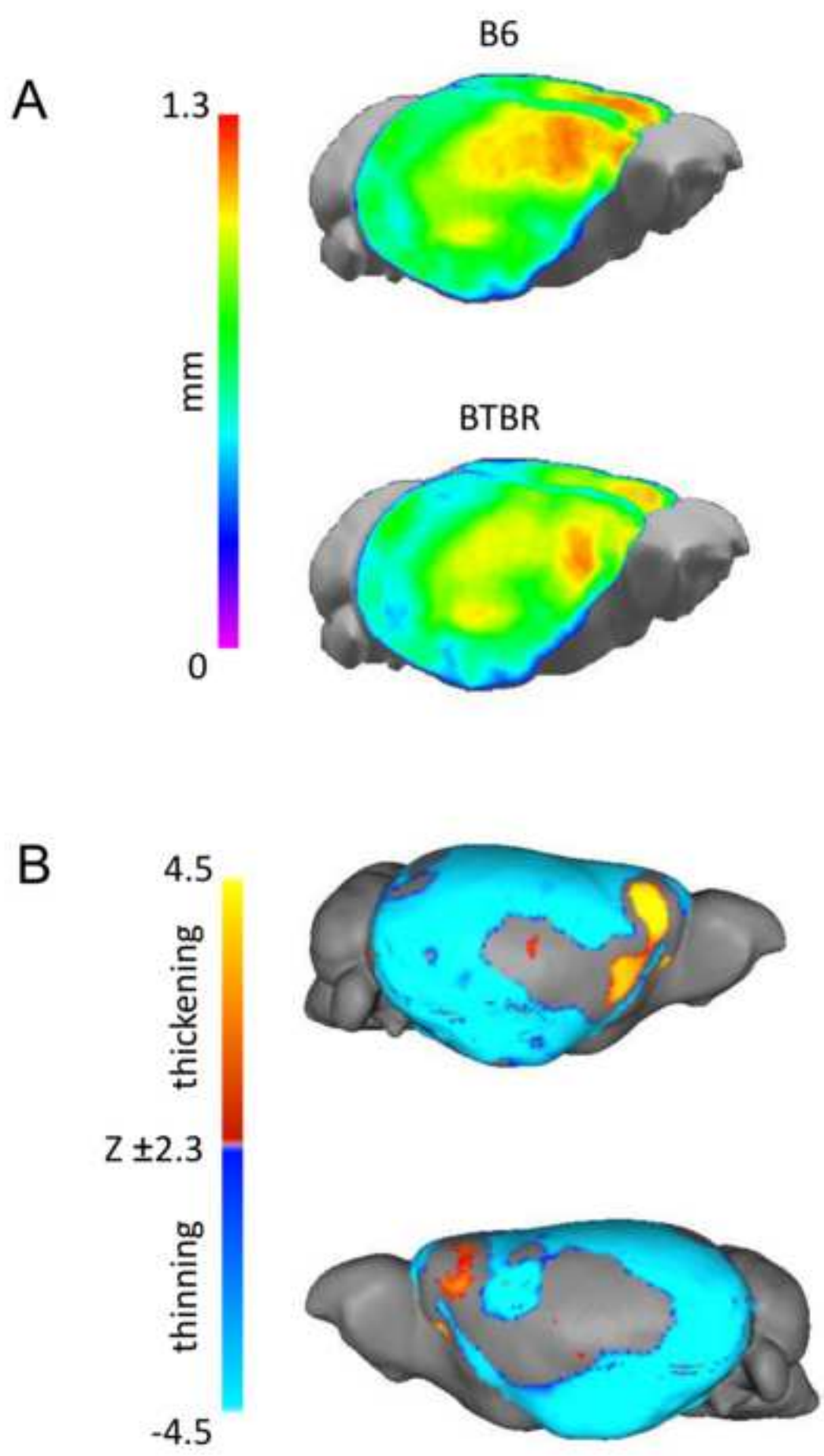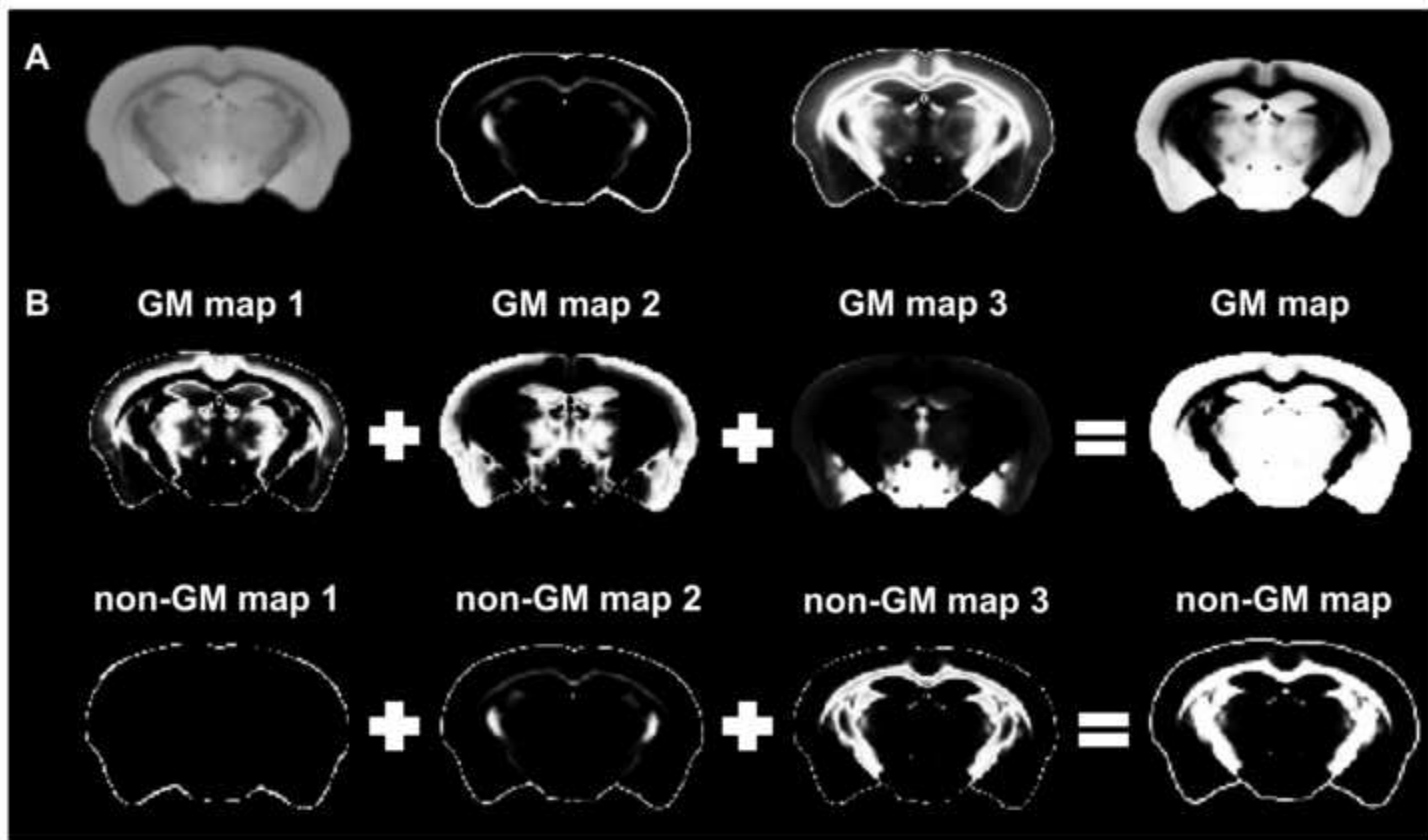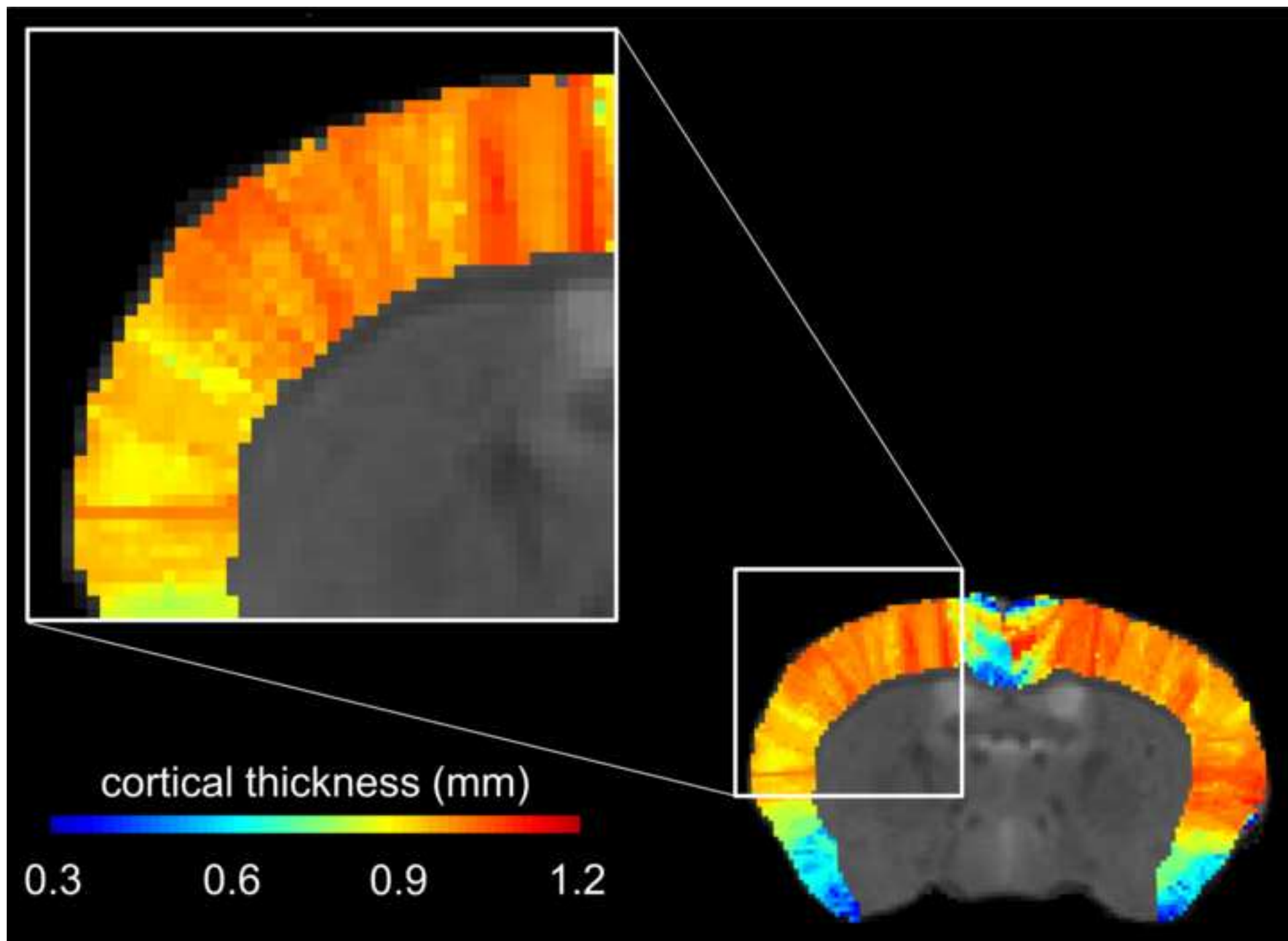**Figure 6**
Click here to download high resolution image

Au
0.75 mm (DiReCT)   0.79 mm (DiReCT)
0.74 mm (manual)   0.78 mm (manual)

S2
1.03 mm (DiReCT)   1.05 mm (DiReCT)
1.01 mm (manual)   1.06 mm (manual)

M2
1.11 mm (DiReCT)   1.09 mm (DiReCT)
1.15 mm (manual)   1.09 mm (manual)

r=0.99
p<0.001

Figure 9
Click here to download high resolution image

cortical thickness (mm)

0.3   0.6   0.9   1.2